JOURNAL OF COLLOID SCIENCE 17, 448–476 (1962)

# THE FLOW OF SUSPENSIONS THROUGH TUBES[1]

## I. SINGLE SPHERES, RODS, AND DISCS

**H. L. Goldsmith[2] and S. G. Mason**

*Physical Chemistry Division, Pulp & Paper Research Institute of Canada, and Department of Chemistry, McGill University, Montreal, Canada*

*Received September 12, 1961*

### List of Symbols

| | |
|---|---|
| $a$ | = semiaxis of revolution of spheroid. |
| $a'(\phi)$ | = projected semiaxis of revolution, Eq. [11]. |
| $b$ | = semiaxis of equatorial diameter of spheroid, radius of rigid sphere and undistorted drop. |
| $b'(\phi)$ | = projected semiaxis of equatorial diameter, Eq. [12]. |
| $B$ | = minor axis of deformed drop. |
| $C$ | = orbit constant. |
| $D, D_B$ | = $(L - B)/(L + B)$ = deformation of fluid drop, deformation at burst. |
| $E, E_B$ | = $Gb\eta_2 f(p)/\gamma$ = ratio of viscous to surface tension forces, $E$ at burst. |
| $f(p)$ | = $(19p + 16)/(16p + 16)$. |
| $f_2(p), f_3(p)$ | = functions of $p$ given by Eqs. [36] and [39], respectively. |
| $F, F_B$ | = $Gb\eta_2/\gamma$; $F$ at burst. |
| $F_{rr}$ | = net force acting on fluid drop. |
| $G, G_B$ | = velocity gradient; $G$ at burst. |
| $G'$ | = effective velocity gradient at center of sphere (Eq. [19]). |
| $k$ | = $4Q/\pi R^4$. |
| $L$ | = major axis of deformed drop. |
| $p$ | = viscosity ratio = $\eta_1/\eta_2$. |
| $p_{rx}$, $p_{ry}$ | = stress components acting on fluid drop. |
| $p(\phi)$ | = steady-state distribution of orientations with respect to $\phi$. |
| $P(\Phi)$ | = integral distribution function, Eqs. [16] and [17]. |
| $P_{x'}(\phi), P_{y'}(\phi)$ | = total components of stress acting on fluid drop (Eq. [26]). |

[1] This work was supported (in part) by research grant H-5911 from the National Heart Institute of the United States Public Health Service.

[2] Holder of a Union Carbide Fellowship (1959–60) and the Spruce Falls Power and Paper Company Limited Fellowship (1960–61).

$Q$ = volume flow rate.
$r$, $\Delta r$ = radial distance from tube axis, difference in $r$.
$r_e$ = equivalent ellipsoidal axis ratio, Eq. [15].
$r_p$ = $a/b$ = particle axis ratio.
$R$ = tube radius.
$s(\phi)$ = $[b'(\phi)]/b = \cos\theta$.
$t$ = time.
$T$ = period of rotation.
$u$, $v$, $w$ = components of fluid velocity along $X$, $Y$, $Z$ axes, respectively.
$u'$ = translational velocity of sphere in $x$ direction (large $b/R$).
$x$, $r$, $\psi$ = cylindrical coordinates.
$X$, $Y$, $Z$ = Cartesian coordinates.
$\gamma$ = interfacial tension.
$\delta$ = $[1 + (2p/5)]D$.
$\epsilon$ = function of $\rho$, $\eta_2$, and $b$, Eq. [27].
$\eta_1$, $\eta_2$ = viscosities of suspended and suspending phases, respectively.
$\theta$ = angle of axis of revolution with $Z$ axis.
$\rho$, $\Delta\rho$ = density and density difference.
$\phi$ = azimuthal angle of axis of revolution.
$\psi$ = polar angle in cylindrical coordinate system.
$\omega$, $\omega'$ = angular velocity, angular velocity of sphere (large $b/R$).

## Introduction

This paper is concerned with the behavior of single particles suspended in liquids undergoing laminar viscous (or Poiseuille) flow through circular tubes. One of the purposes of the work was to compare the translational and rotational motions of rigid particles, such as spheres, discs, and rods, and the deformation of fluid drops with their behavior in Couette flow where experimental results (1–6) are in excellent agreement with theories due to Jeffery (7) and Taylor (8, 9).

Whilst in Couette flow the velocity gradient $G$ is constant, in Poiseuille flow it increases with the radial distance $r$ from the tube axis according to the relation

$$G(r) = \frac{du}{dr} = -kr. \qquad [1]$$

In terms of the cylindrical polar coordinates $r$, $\psi$, and $x$, where $x$ is the polar axis, the field of motion is as shown in Fig. 1. By integration of [1] the component of fluid velocity $u$ in the $x$ direction is

$$u(r) = \frac{k}{2}(R^2 - r^2), \qquad [2]$$

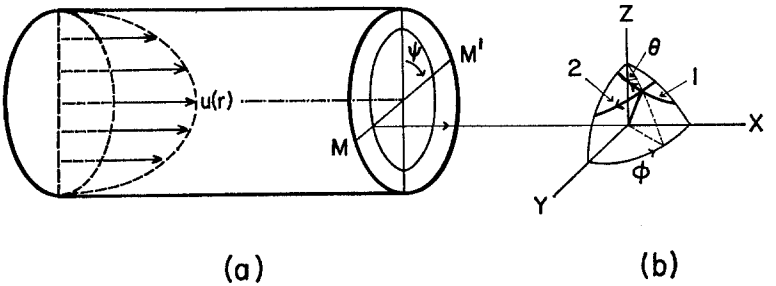


FIG. 1. Coordinate system for Poiseuille flow. (*a*) Cylindrical polar coordinates $r$, $\psi$, $x$. (*b*) Cartesian coordinate system constructed at $x = 0$, $r$, $\psi = -90°$. A spherical elliptical orbit of the axis of revolution of a prolate spheroid ($r_e > 1$) and an oblate spheroid ($r_e < 1$) are shown by curves 1 and 2, respectively.

where $R$ is the tube radius and $k$ a function of the volume rate of flow $Q$:

$$k = \frac{4Q}{\pi R^4}. \qquad [3]$$

A further difference between Couette and Poiseuille flow is that in the former, migration of particles across the planes of shear does not occur (2), whereas in the latter such migration, in a direction away from the tube wall, i.e., towards a lower gradient, has been reported in a number of multiparticle systems (10–12). In some experiments, as in flowing suspensions of red blood cells (13, 14) and pulp fibers (15) axial migration was observed visually. In others (10, 11) it was inferred from the decrease in apparent viscosity with increasing flow rate and decreasing tube radius, an effect which can be explained by the presence of a particle-free layer at the wall of the tube. The formation of this layer has been attributed variously to (*1*) the Magnus effect (16), in which inertial forces normal to the wall act on the particles, and (*2*) to an entrance effect (17) which results in a depletion of particles in the zone adjacent to the tube wall. However, in purely viscous flow and in the absence of particle interactions the theory (7, 18) suggests that the normal forces are zero.

It was therefore considered to be of particular interest to establish whether axial migration of single particles can occur, and to this end very carefully controlled measurements with single rigid spheres, rods, and deformable drops were made.

## EXPERIMENTAL

### *1. General*

The suspensions flowed through 45 cm. lengths of precision bore glass tubing and the particles were viewed through a horizontally or vertically traveling microscope in the median plane ($z = 0$) normal to the viewing axis, i.e., along the $Z$-axis of the field of motion defined in Fig. 1. To elimi-

nate optical distortion by the glass wall a length of the tube passed through a rubber stopper into a square metal glass cell with flat viewing faces on opposite sides and containing a solution (60% dibutyl phthalate and 40% Ucon Oil LB 1715) of the same refractive index as glass ($n_D = 1.474$). This enabled distortion-free viewing inside the tube over a length of 30 cm. The ends of the cell rested in circular slots cut in the steel frame of the traveling microscope and, with the aid of leveling screws, the tube was aligned with the axis of travel to within 0°1′ of the horizontal or vertical. The glass-liquid interface then appeared as a sharp line in the microscope field.

Reproducible flow rates, which could be varied, were obtained by the use of an infusion-withdrawal pump (Harvard Apparatus Co.) driven by a synchronous motor which moved the plunger of a syringe connected to one end of the tube, the other leading to an open reservoir of the suspension. A pair of limit stops actuated a switch which automatically reversed movement of the syringe plunger. For a given syringe, the flow rates were determined by weighing the amount of liquid expelled in a given time and were found reproducible to within 0.3%.

The microscope carriage rested on two vibration-free mounts and by rotation about one end the whole assembly, including the tube, could be inclined at any angle between the horizontal and the vertical. The microscope was driven by a reversible and continuously variable direct-current motor with magnetic amplifier control on a separate vibration-free mount and could be operated at linear speeds ranging from $10^{-3}$ to 2 cm. sec.$^{-1}$. As with the infusion pumps, limit switches reversed the direction of the microscope at each end of its travel. By matching the microscope speed to that of a particle in the tube the latter could be maintained in the center of the field of view and examined for as long as was desired.

The distance traveled by the microscope along the $X$-axis was computed from the readings of a revolution counter, and along the $Y$-axis by a micrometer screw. The particle speed was measured by timing it between two positions of the microscope and the distance of the center from the tube wall ($R - r$) measured with the micrometer screw for separations above 0.15 cm. and with a calibrated micrometer eyepiece for smaller separations. For liquids of refractive index different from glass a correction was applied to give the true ($R - r$); this varied from 0 to 0.25 depending on the liquid and tube radius. Using a 15× eyepiece and 5 cm. objective the resolution for each of the ($x$, $y$, $z$) coordinates was better than 5 microns.

### *2. Materials*

Precision bore glass tubes (Wilmad Glass Co., Buena, New Jersey) of $R = 0.100$ to 0.400 cm. $\pm$ 0.005 cm. were used.

The suspensions of solid and fluid particles studied and their relevant properties are listed in Table I. Systems 1 and 2 were used to study the

TABLE I

*Properties of Suspensions*

(22°C.)

| System | Suspended phase | $b$ ($\mu$) | Axis ratio ($a/b$) | $b/R$ | Suspending phase 2 | $\eta_2$ (*poises*) | $\Delta\rho = \rho_1 - \rho_2$ (*g. cm.*$^{-3}$) | Position of tube |
|---|---|---|---|---|---|---|---|---|
| 1 | Eccospheres[a] | 50 to 150 | 1.0 | 0.013 to 0.038 | Ucon oil LB 1715[b] | 8.41 | 0 | Horizontal |
| 2a | Polystyrene spheres | 450 to 600 | 1.0 | 0.11 to 0.54 | Pale 4 oil[c] | 69.9 | 0.06 | Vertical |
| 2b | Polystyrene spheres | 600 | 1.0 | 0.11 to 0.54 | Ucon oil LB 1715 + 7.9% $CCl_4$ | 5.0 | ±0.002 | Horizontal |
| 3 | Dacron and Terylene rods | 50 to 185 | 6.6 to 31 | 0.013 to 0.046 | Pale 4 oil[c] | 69.9 | 0.38 | Horizontal |
| 4 | Polystyrene discs | 12 to 65 | 0.05 to 0.25 | 0.003 to 0.015 | Pale 4 oil[c] | 69.9 | 0.05 | Vertical |
| 5 | Fibrids[d] | 350 to 500 | 70 to 100 | 0.09 to 0.13 | Glycerol | 6.9 | 0.3 | Vertical |
| 6 | Water | 75 to 300 | 1.0 | 0.002 to 0.07 | Silicone oil[e] 5000 | 50.3 | 0.026 | Horizontal |
| 7 | Water + 0.5% Tween 20[f] | 75 to 300 | 1.0 | 0.002 to 0.07 | Silicone oil[e] 5000 | 50.3 | 0.026 | Horizontal |
| 8 | Pale 4 oil[c] | 75 to 300 | 1.0 | 0.002 to 0.07 | Silicone oil[e] 5000 | 50.3 | 0.026 | Vertical |
| 9 | Oronite[g] | 75 to 300 | 1.0 | 0.002 to 0.07 | Silicone oil[e] 5000 | 50.3 | −0.016 | Horizontal |
| 10 | Pale 4 oil[c] | 75 to 300 | 1.0 | 0.002 to 0.07 | Silicone oil 30,000[e] | 333 | 0.025 | Horizontal |

[a] Hollow glass spheres (Emerson and Cuming, Canton, Mass.).
[b] Union Carbide polyglycol oil.
[c] Oxidized castor oil (Baker Castor Oil Co., New York).
[d] Flexible synthetic bonding fibers (E. I. du Pont de Nemours Co., Wilmington, Delaware).
[e] Dow Corning Silicone fluid.
[f] Polyoxyethylene sorbitan monolaureate o/w emulsifier (Atlas Powder Co., Brantford, Ontario).
[g] Oronite Polybutene 24 (Diversified Research and Sales Ltd., Toronto).

behavior of model spheres, Systems 3 and 4 were used for the rotations of rigid fibers and discs, respectively, and System 5 provided flexible fibers. Systems 6 to 10 were used in the study of the deformation of fluid drops. Rigid fibers of known lengths were prepared from continuous filaments by mounting the strands in embedding wax and cutting them in a sliding microtome. The discs were prepared by compressing polystyrene spheres between the heated platens of a hydraulic press as described elsewhere (6).

With the exception of System 2 the particles were small compared to the tube radius. When appreciable sedimentation of the particles out of the $XY$ plane tended to occur with the tube horizontal, it was set vertically.

For Systems 1, 3, and 5 suspensions of about $10^{-5}$% by weight were used. In Systems 2 and 4 about 25 particles at a time were introduced into 200 ml. of the continuous phase and in Systems 6 to 10 a few liquid droplets were injected directly into the tube with a syringe. Thus in all cases the particle concentrations were so low that interaction effects were negligible.

All experiments were conducted in a constant-temperature room at 22°C. $\pm$ 0.5°. For the liquid droplet systems, strict precautions were taken in the cleaning of all glassware to prevent contamination of the drop interface by impurities. The viscosities of the liquids used were measured in a thermostated (22.00° $\pm$ 0.01°C.) rotational viscometer (Drage Viscometer, A. G. Epprecht, Chemisches Institut, Zurich, Switzerland). With the exception of Oronite, which was slightly viscoelastic, they were found to be Newtonian over the range of gradients employed in the measurements. The interfacial tensions were determined by the ring pull method.

### *3. Rotations*

The period of rotation of spherical particles was measured by following optical imperfections inside the spheres.

The rotations of rods and discs about the $Z$-axis were recorded by using the photomicrograph tape-recorder technique (20). A Robot automatic 35-mm. camera and beam splitter were mounted on the microscope with the $X$-grid line of the ocular aligned with the tube wall. The micrometer eyepiece was mounted on a second beam splitter enabling the position of the particles along the $Y$-axis to be measured. Photographs were taken at various intervals and the time between successive frames obtained from the playback of a tape recording of the audible clicks of the camera shutter. The photographs were projected onto a drafting table and analyzed.

### *4. Deformation of Liquid Drops*

The orientation and deformation of suspended liquid drops were studied at various flow rates using the camera and two beam splitters as above.

The deformation $D$, defined (8) as

$$D = \frac{L - B}{L + B}, \qquad [4]$$

where $L$ and $B$ are the length and breadth of the ellipsoidal drop, was calculated from the length of the main axes of symmetry of the projected image of the drops.

## Results

### *1. Rigid Particles*

*a*). *General Observations.* At the flow rates used in the experiments ($3 \times 10^{-3}$ to 0.14 cm.$^3$sec.$^{-1}$) and over distances up to 3500 cm. traveled by the particles while observations were made, the position of the center of rotation with respect to the tube wall remained constant, even when within one particle diameter of the wall.

The rotation about the $Z$-axis of the spheres in Systems 1 and 2, and of the rods and discs in Systems 3 and 4, were observed to be in agreement with Jeffery's theory (7) for rotating spheroids at the center of an infinite field of Couette flow, that is, laminar fluid motion defined by

$$u = Gy; \qquad v, w = 0, \qquad [5]$$

where $u$, $v$, and $w$ are the respective components of fluid velocity along the $X$, $Y$, and $Z$ axes. The theory predicts that the angular velocities of the axis of rotation in terms of the spherical polar coordinates $\theta$ and $\phi$ with the $Z$-axis as the polar axis, as defined in Fig. 1, are

$$\omega = \frac{d\phi}{dt} = \frac{G}{(r_e^2 + 1)} (r_e^2 \cos^2 \phi + \sin^2 \phi) \qquad [6]$$

$$\frac{d\theta}{dt} = \frac{G(r_e^2 - 1)}{4(r_e^2 + 1)} (\sin 2\phi \sin 2\theta), \qquad [7]$$

where $r_e$ is the axis ratio $a/b$, $2a$ is the length of the axis of revolution, and $2b$ is the equatorial diameter.

It was found that the rotation of the spheres was steady as required by [6], which for $r_e = 1$ reduces to

$$\omega = \frac{G}{2}. \qquad [8]$$

The angular velocity of the rods ($r_p > 1$) was least when the $a$ axis was aligned in the direction of flow and greatest when at right angles corresponding to $\phi = \pi/2$ and 0, respectively, the converse being true of the discs ($r_p < 1$).

The integrated form of [7]

$$\tan \theta = \frac{Cr_e}{(r_e^2 \cos^2 \phi + \sin^2 \phi)^{1/2}} \qquad [9]$$

describes the orbit of each end of the $a$-axis and is a spherical ellipse having the following principal axes:

$$\text{at } \phi = \pi/2 \qquad \tan \theta_1 = Cr_e \qquad [10a]$$

$$\text{at } \phi = 0 \qquad \tan \theta_2 = C \qquad [10b]$$

where $C$ is the orbit constant; $\theta_1$ is the major axis when $r_e > 1$ and the minor axis when $r_e < 1$.

When viewed along the $Z$-axis the projected length $2a'(\phi)$ of the axis of revolution in the $XY$ plane is

$$2a'(\phi) = 2a \sin \theta \qquad [11]$$

and the projection of the equatorial plane is an ellipse of axis ratio $s(\phi) \leqq 1$, where

$$s(\phi) = \frac{b'(\phi)}{b} = \cos \theta \qquad [12]$$

and $b'$ is the projected length of the equatorial diameter at $\phi$. Thus it was found that as the particles rotated the projected length of the rods and the projected axis ratios of the upper face of the discs went from a maximum at $\theta_1$ to a minimum at $\theta_2$.

*b). Spheres. $b/R < 0.04$.* As shown in Fig. 2 the measured translational and angular velocities of the spheres in System 1 at various distances from the tube axis were in good agreement with those calculated from Eqs. [2] and [8], respectively. Based on observations with 25 particles, the mean *measured/calculated* $u(r)$ and $\omega$ were each 1.01. The Poiseuille velocity profile in the tube was thus confirmed.

*$b/R = 0.1$ to 0.5.* The translational ($u'$) and angular velocities ($\omega'$) of the spheres in System 2 were found to be less than those predicted from the streamline velocity ($u$) and velocity gradient ($G$) at the center of the sphere. At a given $a$ and $R$ the slip, defined as $(u - u')/u$ increased with $r$ (Table II). Happel and Byrne (19) have given a relation for the slip at the axis of the tube

$$\left[\frac{(u - u')}{u}\right]_{r=0} = \frac{2}{3}\left(\frac{b}{R}\right)^2 \qquad [13]$$

and by plotting $[(u - u')/u]/[\frac{2}{3}(b/R)^2]$ against $r/R$ it was found, as shown in Fig. 3, that the results obtained in different tubes at various values of $b/R$ lay on a single curve with intercept = 1.0 at the tube axis as required by [13].

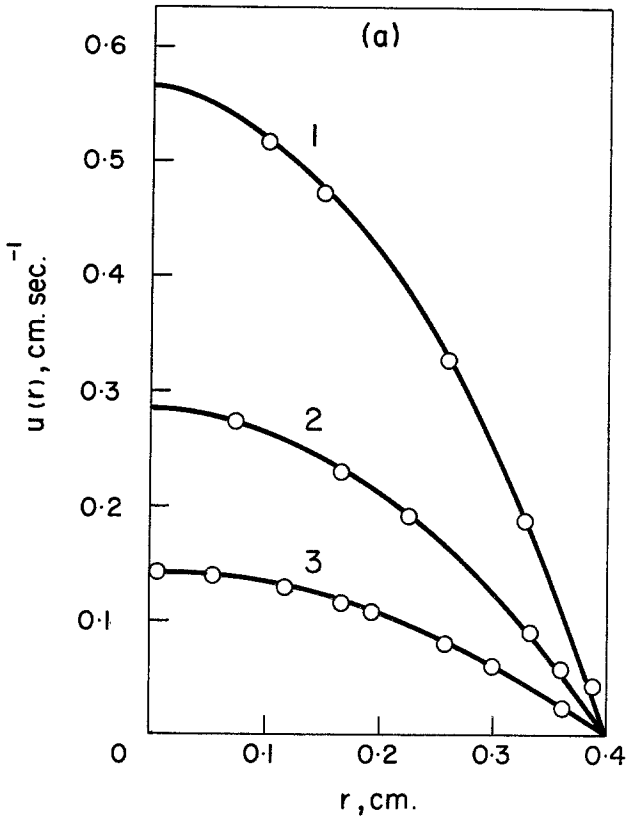


FIG. 2. (*a*) Translational and (*b*) angular velocities of spheres at various flow rates in System 1, $R = 0.400$ cm. The curves are calculated from [2] and [8], respectively. (*1*) $k = 7.08$ cm.$^{-1}$ sec.$^{-1}$; (*2*) $k = 3.54$ cm.$^{-1}$ sec.$^{-1}$; (*3*) $k = 1.77$ cm.$^{-1}$ sec.$^{-1}$.

*c*). *Rods and Discs. Period of rotation.* Equation [6] may be integrated to give

$$\tan \phi = r_e \tan\left(\frac{2\pi t}{T}\right), \qquad [14]$$

where the period of rotation of the spheroid is

$$T = \frac{2\pi}{G}\left(r_e + \frac{1}{r_e}\right). \qquad [15]$$

As found in Couette flow (1–3, 5, 6) the periods of rotation of the rods and discs were less than those predicted when the actual axis ratio $r_p$ was inserted in [15]. This discrepancy was doubtlessly due to deviations from the spheroidal form. Following earlier practice (1) the "equivalent

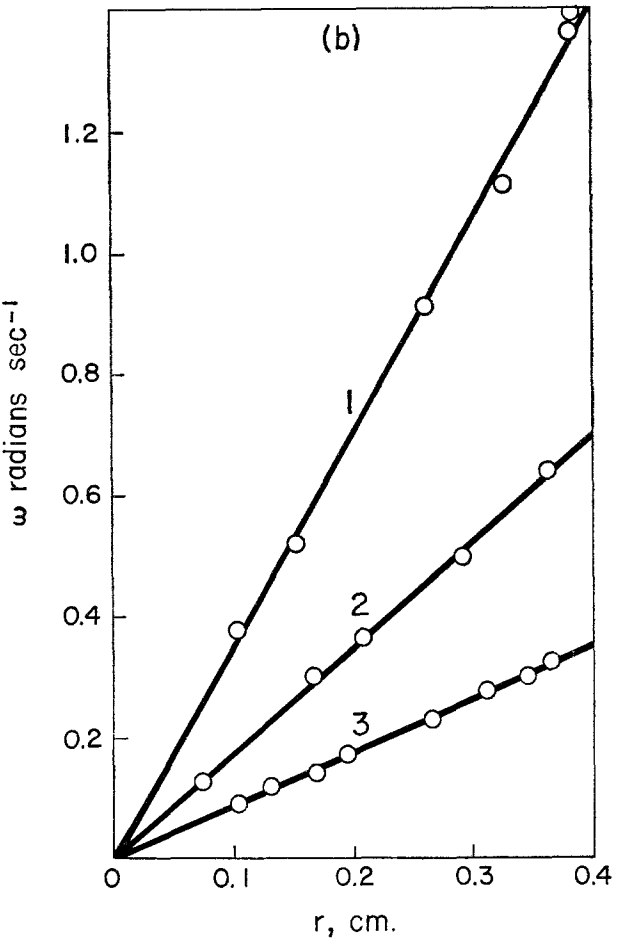


(2b)

ellipsoidal" axis ratio $r_e$ was calculated from [15] by inserting the experimental value of $TG$.

A mean value of $r_p$ was obtained for each sample of rods by direct measurement of about 300 particles under the microscope. For discs, $r_p$ was computed from the measured $b$ and from $a$ calculated from the measured $a'$ and [11], while the particle was rotating in the tube.

The ratios $r_e/r_p$ ($< 1$ for a rod and $>1$ for a disc) decreased with increasing $r_p$ (Table III) as previously found in Couette flow (1, 3, 6).

*Variation of* $\phi$. When the films were analyzed, $\phi$ was measured directly for a rod; for a disc it was given by the angle between the $X$-grid line of the ocular and the major axis $2b$ of the elliptical projection of the upper face.

TABLE II

*Translational Velocities of Large Spheres*

System 2

| $Q$ ($cm.^3 sec.^{-1}$) | $R$ ($cm.$) | $b$ ($cm.$) | $r/R$ | $\frac{u-u'^a}{u}$ | $\frac{b}{R-r}$ |
|---|---|---|---|---|---|
| $3.54 \times 10^{-3}$ | 0.100 | 0.053 | 0 | 0.191 | 0.53 |
| $3.54 \times 10^{-3}$ | | | 0.140 | 0.190 | 0.62 |
| $7.08 \times 10^{-3}$ | | | 0.215 | 0.209 | 0.63 |
| $3.54 \times 10^{-3}$ | | | 0.250 | 0.206 | 0.70 |
| $7.08 \times 10^{-3}$ | | | 0.310 | 0.219 | 0.77 |
| $1.77 \times 10^{-3}$ | | | 0.350 | 0.232 | 0.82 |
| $3.54 \times 10^{-3}$ | | | 0.360 | 0.276 | 0.83 |
| $3.54 \times 10^{-3}$ | | | 0.430 | 0.304 | 0.93 |
| $1.78 \times 10^{-2}$ | 0.200 | 0.046 | 0.175 | 0.044 | 0.50 |
| $1.78 \times 10^{-2}$ | | | 0.248 | 0.049 | 0.53 |
| $1.78 \times 10^{-2}$ | | | 0.370 | 0.057 | 0.57 |
| $1.78 \times 10^{-2}$ | | | 0.480 | 0.069 | 0.61 |
| $1.78 \times 10^{-2}$ | | | 0.548 | 0.076 | 0.63 |
| $1.78 \times 10^{-2}$ | | | 0.630 | 0.118 | 0.68 |
| $7.09 \times 10^{-3}$ | | | 0.723 | 0.211 | 0.83 |
| $3.56 \times 10^{-2}$ | 0.400 | 0.053 | 0.430 | 0.040 | 0.22 |
| $7.12 \times 10^{-2}$ | | | 0.625 | 0.046 | 0.35 |
| $3.56 \times 10^{-2}$ | | | 0.813 | 0.112 | 0.70 |

[a] $u$ is streamline velocity at center of sphere (Eq. [2]). $u'$ is measured velocity of sphere.

The variation of $\phi$ with time is shown in Fig. 4 and compared with Jeffery's theory. A more critical test of the theory is provided by plotting $\tan \phi$ against $\tan (2\pi t/T)$; this has been done in Fig. 5 for a rod and disc and in each case yields excellent agreement with [14].

The steady-state distribution of orientations with respect to $\phi$ for two dilute suspensions of rods was measured after several hours of flow by taking photographs of successive portions of the suspensions at a fixed position along the tube. The value of $\phi$ was measured for those particles appearing in view when the frames were projected onto the drafting table. The corresponding integral distributions, $P(\Phi)$, defined as

$$P(\Phi) = \int_0^{\phi} p(\phi)\, d\phi, \qquad [16]$$

where $p(\phi)\, d\phi$ is the fraction oriented in the interval $d\phi$ at $\phi$, were determined for population of about 500 particles and are compared with values calculated from the theoretical equation (2) based on Eq. [14]:

$$P(\Phi) = \frac{1}{2\pi} \tan^{-1} (\tan \phi / r_e) \qquad [17]$$

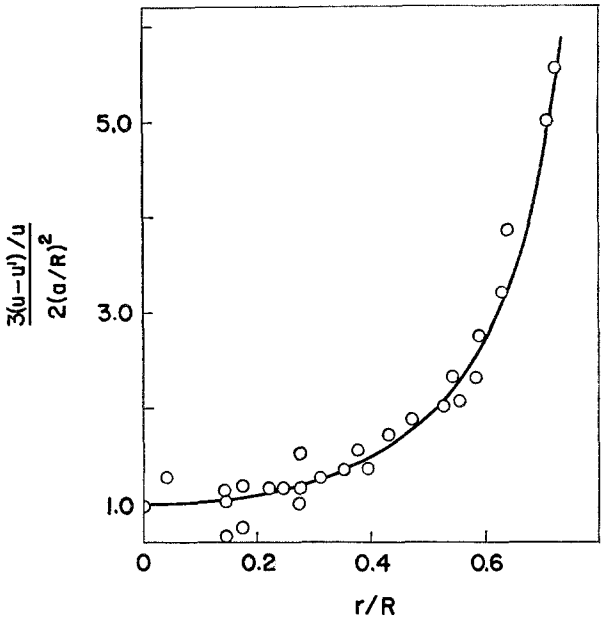


FIG. 3. A plot of $[(u - u')/u]/[\frac{2}{3}(b/R)^2]$ against $r/R$ in System 2; $u'$ is the measured translational velocity, $u$ is the streamline velocity at the center of the spheres given by [2]. The intercept at the tube axis is 1.0 as required by [13].

TABLE III

*Measured and Equivalent Axis Ratios for Rods and Discs*

| System | $TG/2\pi$ (measured) | $r_e$ (Eq. [15]) | $C$ (Eq. [10]) | $r_p$[a] | $r_e/r_p$ |
|---|---|---|---|---|---|
| 4 | 5.64 | 0.183 | 0.35 | 0.09 | 2.1 |
| | 4.60 | 0.227 | ∞ | 0.12 | 1.9 |
| | 4.64 | 0.226 | 0.27 | 0.12 | 2.2 |
| | 4.66 | 0.226 | 2.94 | 0.13 | 1.7 |
| | 2.06 | 0.862 | 1.67 | 0.69 | 1.2 |
| 3 | 4.99[b] | 4.78[b] | | 6.6[b] | 0.72 |
| | 21.3[b] | 21.2[b] | | 31[b] | 0.69 |

[a] Particle axis ratio.

[b] Mean value for the suspension.

in Fig. 6; a set of values for Couette flow (20) is included. It may be seen that the distribution obtained in Poiseuille flow is closer to theory than that in Couette flow.

*Variation of* $\theta$. With the aid of the following relation, derived from [9]

$$\sin \theta_1 = \left[\frac{r_e^2 - [a'(\pi/2)/a'(0)]^2}{(r_e^2 - 1)}\right]^{1/2}, \qquad [18]$$

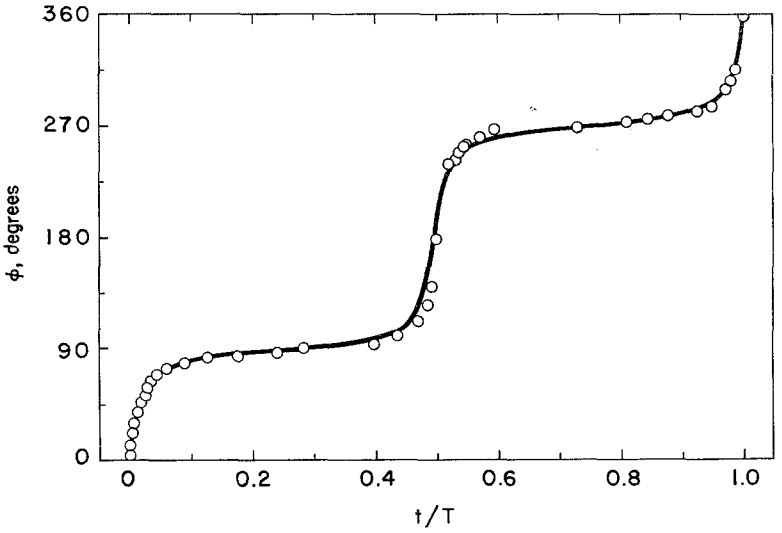


FIG. 4. Variation of $\phi$ with time for a rigid rod $r_e = 20.6$, $G = 0.31$ sec.$^{-1}$. The line is calculated from [14].

and, by means of [10] and [11], $\theta$ for a rod was calculated from the measured $a'(\phi)$; for a disc it was computed from the measured $s(\phi)$ using [12].

Contrary to [9] the variation of $\theta$ with $\phi$ for rods and discs was not identical in the two successive half orbits $\phi = -\pi/2$ to $\pi/2$ and $\phi = \pi/2$ to $-\pi/2$ as shown by differences in the respective values of $a'(0)$ and $s(0)$. Similar but smaller differences were observed between the values of $a'$ and $s$ at $\phi = -\pi/2$ and $\pi/2$. The effect is illustrated in Fig. 7 for a rod and a disc, respectively, where tan $\theta$ has been plotted against $\phi$ and the lines drawn calculated from [9] using the orbit constant $C$ obtained from the $a'(0)$ and $s(0)$ in the first half orbit. In both cases the points obtained in the second half orbit lie below the line. This result was undoubtedly due to a lack of perfect symmetry in the particles. This would cause a reversible precession of the orbit from one half rotation to the next.

*d). Wall Effects. Spheres.* Vand (21, 22) has calculated the interaction between a sphere and a rigid wall in a liquid undergoing Couette flow. Using the method of reflections (23) the effective velocity gradient $G'$ at the center of the sphere was found to be

$$G' = G\left(1 + \frac{5}{16}\left(\frac{b}{R-r}\right)^3 - \frac{1}{8}\left(\frac{b}{R-r}\right)^5 + \cdots\right)^{-1}, \qquad [19]$$

where $G$ is the velocity gradient of the undisturbed fluid at $(R - r)$. Values of $\omega'$ calculated from $G'$ given by [19], neglecting terms of $b/(R - r)$ higher than the third power, are compared with the measured values for

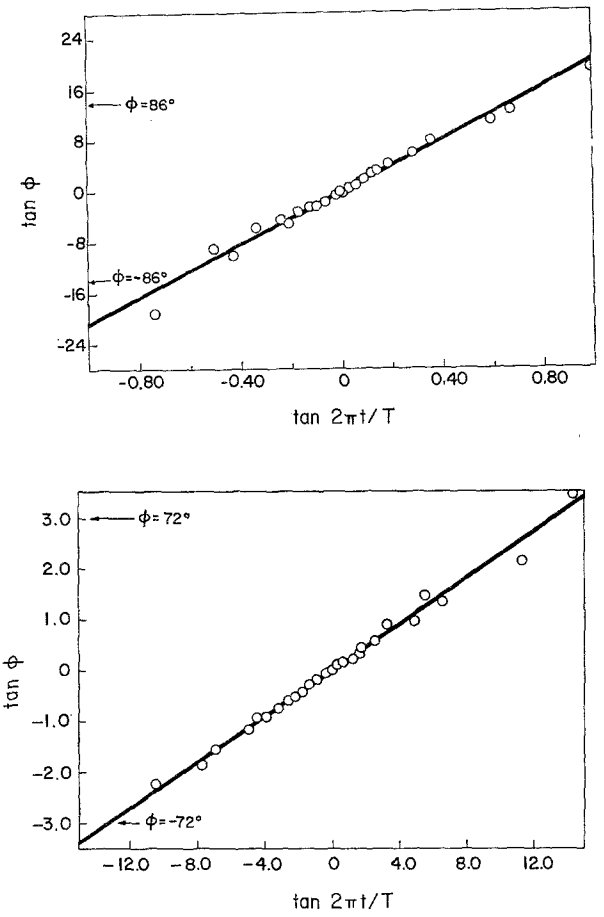


FIG. 5. Tan $\phi$ vs. tan $(2\pi t/T)$ for a rod (*upper*) and a disc (*lower*). The rod is the same particle as in Fig. 4. For the disc, $r_e = 0.226$ and $G = 0.22$ sec.$^{-1}$. The straight lines drawn are given by [14] using the corresponding values of $r_e$.

spheres within one diameter of the tube wall in Table IV. The agreement is good except when the center of rotation was close to one particle radius from the tube wall; in this case it was found that $\omega'(\text{meas.})/\omega'(\text{calc.})$ decreased with increasing $r$, in a region where approximations of the theory would not be expected to hold.

*Rods and discs.* With rods whose centers of rotation were within a distance $a$ of the tube wall the values of $r_e$ obtained from the measured $TG$ and designated as $(r_e)_{TG}$ were much greater than the mean $r_e$ for the suspension, whereas the values of $r_e$, designated as $(r_e)_\phi$, obtained from the linear plot of tan $\phi$ vs. tan $(2\pi t/T)$ between $\phi = -86°$ and $+86°$ were within the variation in $r_e$ observed for the suspension. This indicated that the

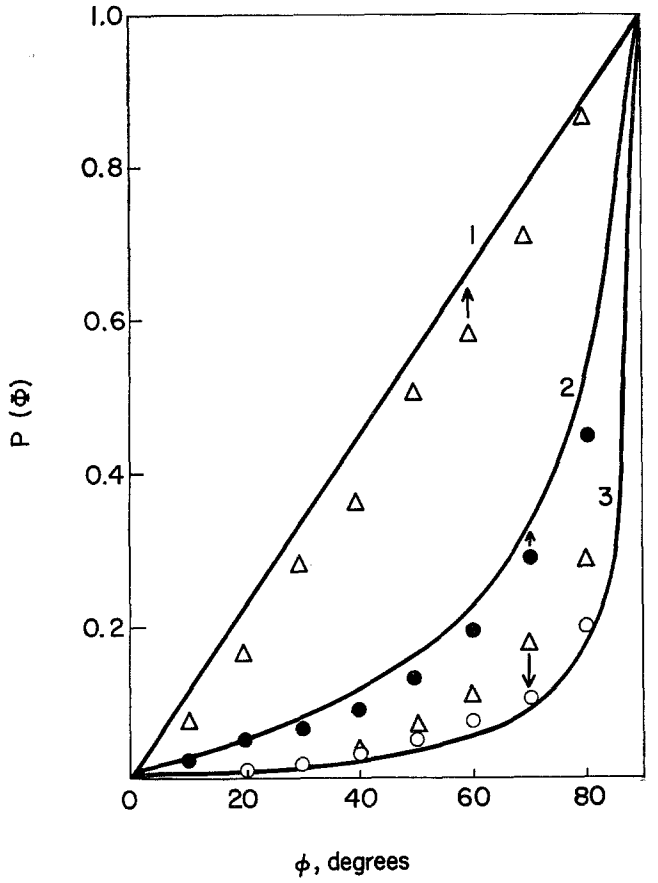


FIG. 6. Steady-state distribution of orientations with respect to $\phi$ for suspensions of rigid rods. *Curve 1.* Initial isotropic distribution. The triangles are experimental points at time $t = 0$ obtained in Couette flow (20). *Curve 2.* Calculated from [17] for $r_e = 6.60$. Closed circles are experimental points obtained in Poiseuille flow after 60 rotations/particle. *Curve 3.* Calculated from [17] for $r_e = 20.8$. The triangles are experimental points obtained in Couette flow after 1600 rotations/particle (20); open circles are points obtained in Poiseuille flow after 60 rotations/particle.

interaction with the wall was confined to that part of the orbit between $\phi = 90° \pm 4°$ where the particles (mean $r_e = 20.8$) spent 90% of their time and where they were nearly aligned with the flow. The measured $a'(0)$ showed that when aligned at right angles to the flow the particles did not come into contact with the wall. These results together with the respective values of $r_e/r_p$ are given in Table V.

With discs of the same axis ratio $r_p$ whose centers of rotation were within one equatorial diameter of the wall $TG$ increased, and hence $r_e$ decreased, with increasing $r$ (Table V).

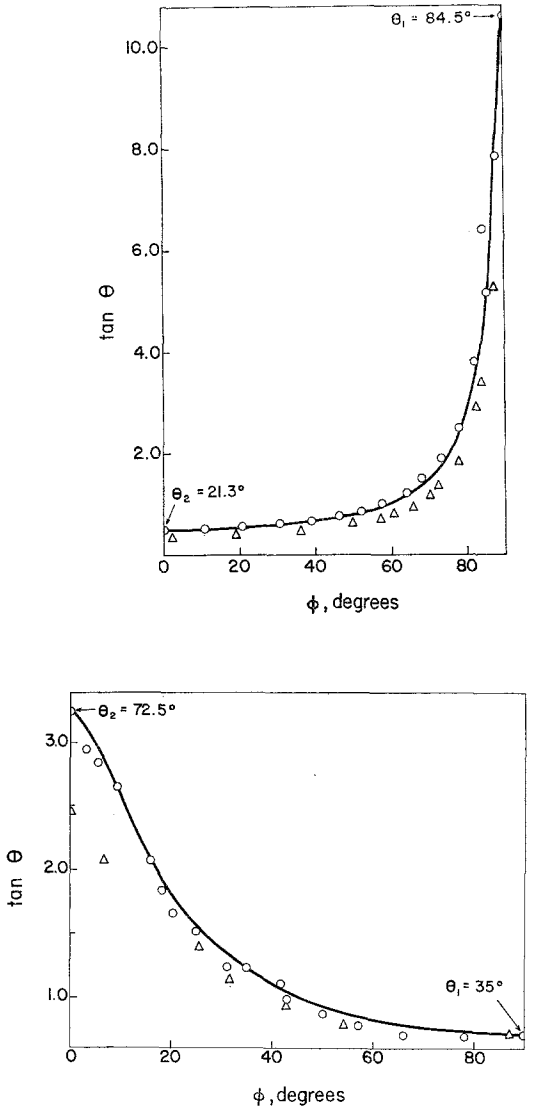


FIG. 7. Tan $\theta$ vs. $\phi$ for a rigid rod (*upper*) and a disc (*lower*). *Rod:* $r_e = 20.6$, $G = 0.31$ sec.$^{-1}$. The curve is calculated from [9] using $C = 0.52$ obtained from $a'(-\pi/2)/a'(0)$. *Disc:* $r_e = 0.226$, $G = 0.22$ sec.$^{-1}$. The curve is calculated from [9] using $C = 2.93$ obtained from $s(0)$. In both cases the open circles are experimental values obtained in the half orbit $\phi = -\pi/2$ to $\pi/2$ and the triangles are values obtained in the following half orbit.

### *2. Liquid Drops*

*a*). *General Observations.* In all systems studied the drops migrated towards the tube axis during flow, the rate of migration increasing with increasing drop radius, flow rate, and radial distance.

TABLE IV

*Wall Effects in the Rotation of Spheres*

System 2

| $Q$ ($cm.^3 sec.^{-1}$) | $R$ ($cm.$) | $b$ ($cm.$) | $\frac{b}{R-r}$ | $\omega'$ measured ($radians\ sec.^{-1}$) | $\omega'^a$ calculated ($radians\ sec.^{-1}$) | $\frac{\omega'^b}{\omega}$ |
|---|---|---|---|---|---|---|
| $3.54 \times 10^{-3}$ | 0.100 | 0.0390 | 0.624 | 0.78 | 0.79 | 0.92 |
| $3.54 \times 10^{-3}$ | | 0.0515 | 0.691 | 0.54 | 0.52 | 0.94 |
| $3.54 \times 10^{-3}$ | | 0.0515 | 0.705 | 0.56 | 0.55 | 0.92 |
| $7.08 \times 10^{-3}$ | | 0.0515 | 0.746 | 1.25 | 1.23 | 0.90 |
| $3.54 \times 10^{-3}$ | | 0.0530 | 0.779 | 0.62 | 0.62 | 0.86 |
| $1.77 \times 10^{-3}$ | | 0.0515 | 0.792 | 0.35 | 0.34 | 0.87 |
| $3.54 \times 10^{-3}$ | | 0.0530 | 0.815 | 0.68 | 0.67 | 0.85 |
| $3.54 \times 10^{-3}$ | | 0.0530 | 0.828 | 0.69 | 0.69 | 0.84 |
| $3.54 \times 10^{-3}$ | | 0.0515 | 0.904 | 0.69 | 0.79 | 0.78 |
| $1.78 \times 10^{-2}$ | 0.200 | 0.0460 | 0.508 | 0.73 | 0.74 | 0.95 |
| $7.09 \times 10^{-3}$ | | 0.0425 | 0.512 | 0.80 | 0.79 | 0.96 |
| $1.78 \times 10^{-2}$ | | 0.0525 | 0.568 | 0.72 | 0.72 | 0.96 |
| $1.78 \times 10^{-2}$ | | 0.0470 | 0.635 | 0.83 | 0.82 | 0.93 |
| $7.09 \times 10^{-3}$ | | 0.0460 | 0.829 | 0.34 | 0.35 | 0.82 |
| $3.56 \times 10^{-2}$ | 0.400 | 0.0530 | 0.720 | 0.54 | 0.51 | 0.94 |
| $3.56 \times 10^{-2}$ | | 0.0490 | 0.923 | 0.46 | 0.44 | 0.77 |
| $3.56 \times 10^{-2}$ | | 0.0540 | 0.947 | 0.42 | 0.48 | 0.69 |
| $3.56 \times 10^{-2}$ | | 0.0540 | 0.982 | 0.41 | 0.47 | 0.67 |
| $3.56 \times 10^{-2}$ | | 0.0540 | 0.991 | 0.39 | 0.47 | 0.64 |
| $3.56 \times 10^{-2}$ | | 0.0540 | 1.000 | 0.32 | — | 0.52 |

$$\text{Mean } \frac{\omega' \text{ (measured)}}{\omega' \text{ (calculated)}} = 0.98$$

[a] From [8] using $G$ calculated from [19].

[b] Calculated from the measured $\omega'$ and $\omega$, computed from $G$ at the center of the sphere using [8].

Apart from this migration across the planes of shear the behavior of the drops was similar in all respects to that observed in Couette flow (5). At low gradients they were deformed into prolate spheroids with the major axis initially aligned at $\phi_m = +\pi/4$, with the deformation and $\phi_m$ increasing with $G$. When tiny liquid droplets of the continuous phase were present inside the drops, internal circulation could be observed. To reduce the gradient in $G$ across the ends of the particles the experiments were carried out at ratios of $b/R < 0.07$. The maximum $Gb$ that would then be obtained was too small to observe bursting of the drops (5) in Systems 6 and 7, but observations with larger drops in System 7 ($b/R > 0.2$) showed that at the bursting gradient $G_B$ they assumed the sigmoidal shape with pointed ends characteristic of Class A deformation at break-up (5). In

TABLE V

*Wall Effects in the Rotation of Rods and Discs*

$R = 0.400$ cm.

| System | $(R - r)$ ($\mu$) | $a^a$ ($\mu$) | $b^b$ ($\mu$) | Axis ratio $r_p = a/b$ | $(r_e)_{TG}$ | $(r_e)_\phi$ | $\frac{(r_e)_{TG}}{r_p}$ | $\frac{(r_e)_\phi}{r_p}$ | $a'(0)$ ($\mu$) |
|---|---|---|---|---|---|---|---|---|---|
| 3 | 75 | 185 | 6 | 31 | 24.2 | 17.0 | 0.78 | 0.55 | 60 |
| $r_e = 20.8 \pm 4.0$ | 90 | 225 | 6 | 37 | 29·7 | 25.5 | 0.80 | 0.68 | 70 |
| $r_p = 31 \pm 6$ | 145 | 160 | 6 | 27 | 18.0 | — | 0.67 | — | — |
| | 490 | 175 | 6 | 29 | 20.6 | 20.6 | 0.71 | 0.71 | 90 |
| 4 | 475 | 125 | 735 | 0.18 | 0.202 | — | 1.2 | — | — |
| | 605 | 125 | 735 | 0.18 | 0.267 | — | 1.6 | — | — |
| | 735 | 125 | 735 | 0.18 | 0.275 | — | 1.7 | — | — |
| 4 | 525 | 125 | 830 | 0.15 | 0.221 | — | 1.5 | — | — |
| | 620 | 125 | 830 | 0.15 | 0.235 | — | 1.6 | — | — |
| | 820 | 125 | 830 | 0.15 | 0.240 | — | 1.6 | — | — |

[a] System 3: calculated from $(r_e)_\phi$ using [18] and [11].
System 4: calculated from the measured $a'(0)$ using [11].

[b] System 3: mean value for the suspension.
System 4: measured value.

System 8, $G_B$ was lower and break-up was observed with the smaller drops, and occurred at the center of the particles as previously described for Class B-1 at burst (5).

*b*). *Variation of D.* The variation of $D$ with $Gb$ was measured in Systems 7 to 10, the experiments being conducted quickly so that axial migration could be neglected. The results are illustrated in Fig. 8. At low values of $D$ the increase was linear as required by the theory of Taylor (9) in which $D$ is given by

$$D = F \cdot f(p), \qquad [20]$$

where $p$ is the viscosity ratio $(\eta_1/\eta_2)$ of drop to continuous phase and

$$F = \frac{Gb\eta_2}{\gamma}, \qquad f(p) = \frac{19p + 16}{16p + 16}. \qquad [21]$$

The values of the interfacial tension calculated from the initial slopes of the best-fit lines through the experimental points, using [20], showed good agreement with those directly measured (Table VI). As $D$ increased, negative deviation from [20] was found in System 10 and positive deviation in System 8, as observed in Couette flow (5). In System 9, $D$ at a given $G$ decreased markedly with time while $\phi_m$ remained constant, angles as high as 89° being obtained at $D = 0.1$. Axial migration during the time of the experiments was too small to account for this decrease in $D$, and it

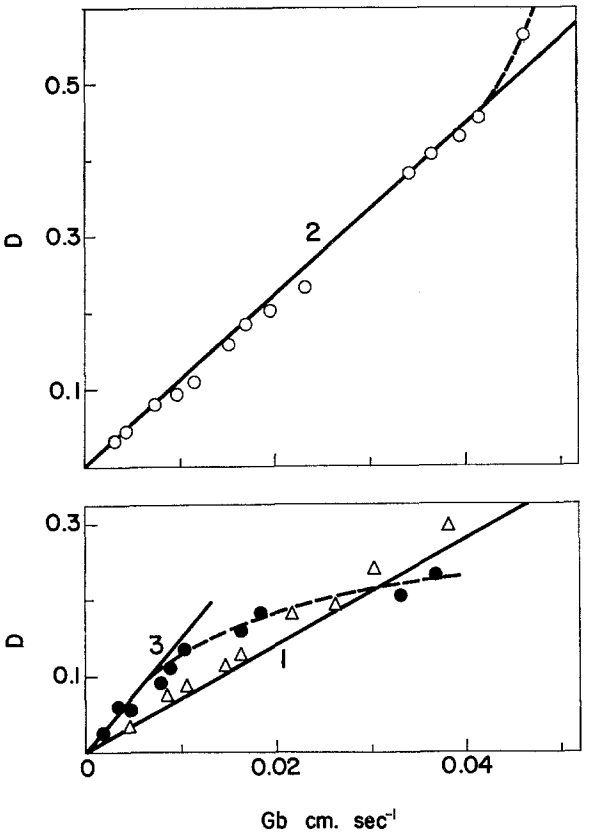


FIG. 8. Deformation of liquid drops in Poiseuille flow; plot of $D$ vs. $Gb$. (*1*) System 7, Class A deformation; experimental points are triangles. (*2*) System 8, Class B deformation. (*3*) System 10, Class C deformation. The full lines drawn are calculated from [20] using the measured values of $p$, $\eta_2$, and $\gamma$.

must be concluded that the interface experienced an aging effect which changed its mechanical properties.

If [20] applies at higher values of $D$ it can be shown (5, 9) that the critical deformation above which the drop will burst is given by

$$D_B = \tfrac{1}{2}. \qquad [22]$$

Break-up in System 8 was observed at $D = 0.55$ and the corresponding value of $F_B \cdot f(p)$ calculated from [20] was 0.55, close to the predicted value of 0.5.

*c*). *Variation of* $\phi_m$ . The variation of $\phi_m$ with $Gb$ is illustrated in Fig. 9, and is compared with the theory of Cerf (24) for small deformations. As a result of rotation of the drop and the consequent strain relaxation, $\phi_m$

TABLE VI

*Deformation of Fluid Drops*

| System | Deformation class[a] | $p = \eta_1/\eta_2$ | $\gamma$ (*dyne cm.*$^{-1}$) Meas. | $\gamma$ (*dyne cm.*$^{-1}$) Eq. [20] | $\phi_{m,B}$ | $\frac{d^2D}{d(Gb)^2}$ |
|---|---|---|---|---|---|---|
| 6 | A | $2 \times 10^{-4}$ | 29.0 | 25[a] | | |
| 7 | A | $2 \times 10^{-4}$ | 7.4 | 7.3 | | |
| 8 | B | 1.39 | 4.9 | 5.0 | 75 | + |
| 10 | C | 4.8 | 5.4 | 6.7 | | − |

[a] From reference 5.

is predicted to vary according to the relation

$$\phi_m = \frac{\pi}{4} + \left(1 + \frac{2p}{5}\right) D. \qquad [23]$$

The experimental data agree with [23] especially at low $D$ as was previously found for Couette flow (5).

### 3. *Axial Migration*

Studies of the axial migration of single rigid and deformable particles were made at various flow rates in a vertical tube ($R = 0.4$ cm.) so as to avoid sedimentation out of the $XY$ plane.

*a*). *Rigid Spheres and Rods.* Continuous experiments were carried out over a period of 18 to 24 hours with spheres and rods whose centers of rotation were within one particle axis of the tube wall with the results shown in Table VII.

With spheres it was found that even after traveling $6.5 \times 10^4$ particle radii (3500 cm.) they had moved less than 0.06 $b$ ($< 30$ microns) away from the wall. For those spheres which had moved out from the wall the periods of rotation had decreased (Table VII).

With rods no migration was observed over distances of travel from 300 to 1200 cm. Further, it was noted that when a suspension of rods flowed continuously over 48 hours many particles whose centers of rotation were within a distance $a$ of the tube wall were visible.

*b*). *Deformable Drops.* A study of the migration of drops was made in Systems 6, 7, 8, and 10. The results for System 6 are shown in Table VIII and Fig. 10, where $r$ has been plotted against time. It is evident that axial migration was appreciable at all flow rates and particle radii, in striking contrast to the behavior of the rigid particles described above. The results show increasing rates of migration with increase in $b$, $r$, and $Q$ and in these experiments ranged from 0.2 to 11 microns/sec.

The reasons for this difference in behavior of rigid and fluid particles are discussed below.

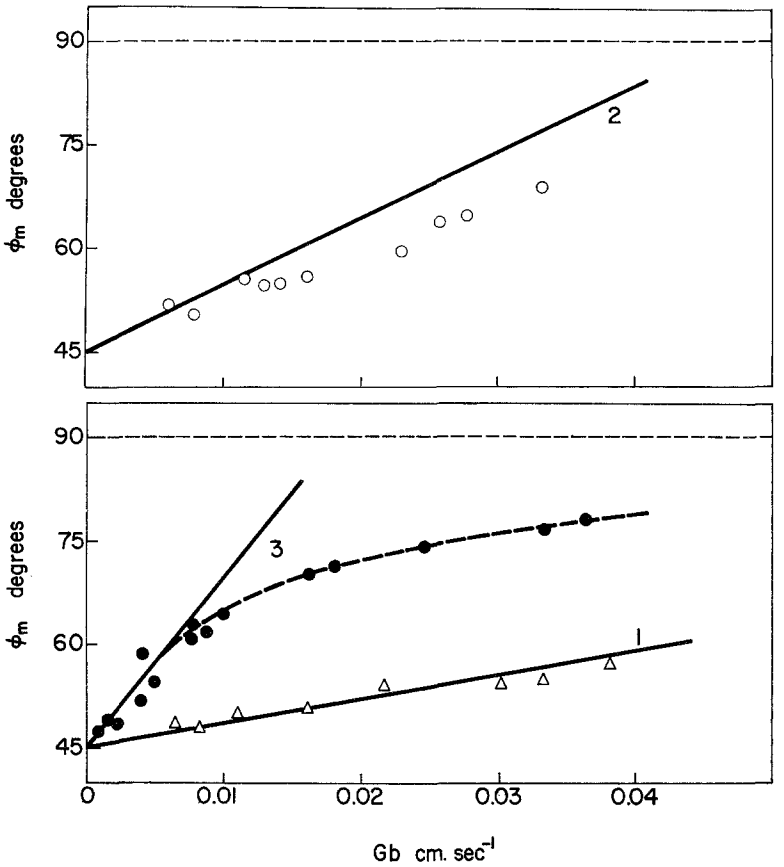


FIG. 9. Variation of $\phi_m$ with $Gb$. (*1*) System 7 (Class A). (*2*) System 8 (Class B) (*3*) System 10 (Class C). The full lines drawn are calculated from [23] using the measured values of $p$, $\eta_2$, and $\gamma$ to calculate $D$ from [20].

*c*). *Flexible Fibers.* A few experiments were carried out with the flexible fibers of System 5. It was observed that at a given velocity gradient the flexibility of the fibers varied from particle to particle. Some were observed to rotate in springy orbits (4, 15), the fiber bending under compression in the quadrant $-90° < \phi < 0°$ and relaxing again in the following quadrant $0° < \phi < 90°$. In others the two ends were capable of independent movement as in snake orbits (15). In both cases axial migration was observed; at a flow rate of 0.0712 cm.$^3$sec.$^{-1}$ the initial rates of migration increased from 0.05 to 0.1 $\mu$/second as the flexibility increased.

## DISCUSSION

The results have shown that with the exception of effects due to interaction with the wall and neglect of particle size, the behavior of the model

TABLE VII

*Axial Migration of Rigid Spheres*

$R = 0.400$ cm.

| System | $Q$ ($cm.^3$ $sec.^{-1}$) | Particle | $b$ ($\mu$) | $(R-r)$ after $\frac{\Delta x}{b}$ particle radii of travel (*microns*) | | | | Total $\frac{\Delta r}{b}$ particle radii | $T$ after $\frac{\Delta x}{b}$ particle radii of travel (*seconds*) | | | |
|---|---|---|---|---|---|---|---|---|---|---|---|---|
| | | | | $\frac{\Delta x}{b}=0$ | $1.5\times10^4$ | $2.2\times10^4$ | $6.5\times10^4$ | | $\frac{\Delta x}{b}=0$ | $1.5\times10^4$ | $2.2\times10^4$ | $6.5\times10^4$ |
| 2 | 0.0356 | 1 | 540 | 550 | 555 | | | −0.009 | 31.4 | 31.5 | | |
| | | 2 | 540 | 550 | 550 | | | 0 | 31.8 | 31.5 | | |
| | | 3 | 540 | 540 | 550 | | | −0.019 | 38.9 | 31.2 | | |
| 2 | 0.0712 | 4 | 540 | 570 | 560 | 560 | 570 | 0 | 15.0 | 15.0 | 15.0 | 15.0 |
| | | 5 | 540 | 545 | — | 565 | 575 | −0.056 | 16.1 | — | 14.6 | 14.1 |
| | | 6 | 530 | 540 | 560 | — | 570 | −0.056 | 15.4 | — | 15.1 | 14.3 |
| | | 7 | 490 | 535 | 540 | 540 | 550 | −0.030 | 13.6 | 13.5 | 13.6 | 13.3 |

TABLE VIII

*Axial Migration of Deformable Drops*

$R = 0.400$ cm.

System 6

| Flow rate ($cm.^3$ $sec.^{-1}$) | $b$ (*cm.*) | $r_0^a$ (*cm.*) | $-dr/dt$ ($\mu$/*sec.*) initial | | $-\Delta r/b$ after $x$ cm. of travel, $x$ = | | | | $D^b$ | |
|---|---|---|---|---|---|---|---|---|---|---|
| | | | Meas. | Calc.[c] | 50 | 100 | 150 | 200 | Initial | After $x$ = 150 cm. |
| 0.0356 | 0.0175 | 0.289 | 0.15 | 0.08 | 0.48 | 0.84 | 1.16 | 1.43 | 0.026 | — |
| | 0.0300 | 0.296 | 0.46 | 0.38 | 1.03 | 1.68 | 2.18 | 2.59 | 0.039 | 0.030 |
| | 0.0390 | 0.268 | 0.93 | 0.76 | 1.13 | 1.80 | 2.30 | 2.70 | 0.055 | 0.032 |
| 0.0712 | 0.0410 | 0.261 | 3.80 | 3.45 | 1.68 | 2.48 | 3.09 | — | — | — |
| 0.142 | 0.0350 | 0.292 | 11 | 9.68 | 3.00 | 3.80 | 4.42 | — | 0.13 | 0.12 |

[a] Initial radial distance.

[b] From [4].

[c] From [37].

rigid spheres and spheroids in Poiseuille flow was similar to that found in Couette flow (1–4, 6) and could be described by the theory of Jeffery (7). In the case of rods and discs there was no evidence that the particles assumed positions and orbits leading to minimum dissipation of energy, i.e., axial concentration towards the region of $G = 0$ and drift of orbits to $C = 0$ for a rod and $C = \infty$ for a disc, as Jeffery (7) suggested might occur.

The deformation and burst of liquid drops were the same as in Couette flow (5) and were in quantitative agreement with the theory for small deformation (8, 9, 24).

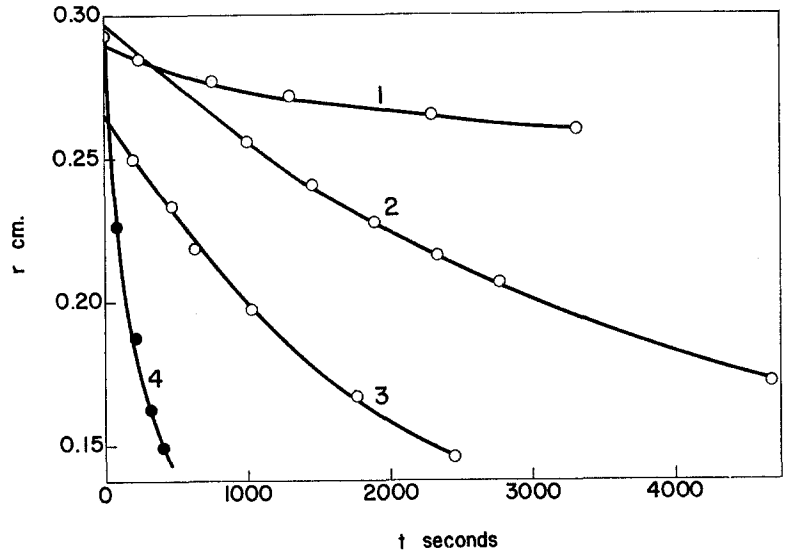


FIG. 10. Axial migration of fluid drops in a tube $R = 0.4$ cm.: plot of $r$ vs. time Open circles: flow rate = 0.0356 cm.$^3$ sec.$^{-1}$; closed circles: flow rate = 0.142 cm.$^3$ sec.$^{-1}$. The numbered curves represent drops of radii (*1*) 175 $\mu$, (*2*) 300 $\mu$, (*3*) 390 $\mu$, (*4*) 350 $\mu$.

It thus remains only to consider the mechanism of axial migration of deformable drops and to explain its absence with rigid particles. This can be done by calculating the net radial force acting on a particle as a result of the variation of $G$ across it. An approximate analysis is presented below.

Consider a particle undergoing deformation in Poiseuille flow as shown in Fig. 11. The variation in $G$ across the particle is from [1]

$$G = G_0 + ky', \qquad [24]$$

where the gradient at the center of the particle ($y' = 0$) is

$$G_0 = -kr,$$

$k$ being defined by [3], $r$ being the radial distance of the particle center, the $x$, $y$ coordinates having been replaced by $x'$, $y'$. The drop experiences compressive and tensile forces normal to its surface in the manner shown in Fig. 11. From the theory of Taylor (8) for small deformation of liquid drops it can be shown that the stress components $p_{rx'}$ and $p_{ry'}$ in Couette flow in spherical polar coordinates are given by

$$p_{rx'} = \frac{5p\eta_2 G}{2(p+1)}\left[1 + \frac{16}{5p}\sin^2\theta \sin^2\phi\right]\sin\theta\cos\phi; \qquad [25a]$$

$$p_{ry'} = \frac{5p\eta_2 G}{2(p+1)}\left[1 + \frac{16}{5p}\sin^2\theta \cos^2\phi\right]\sin\theta\cos\phi. \qquad [25b]$$

We wish to calculate the total stress components at various angles $\phi$.

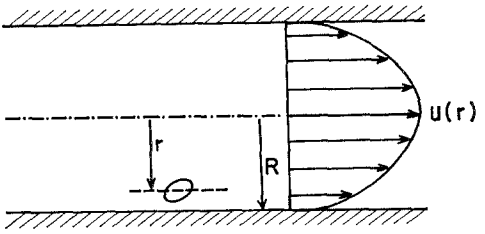


(a)

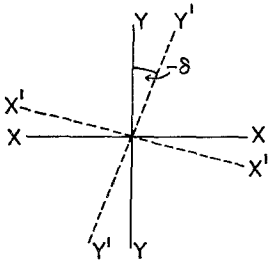


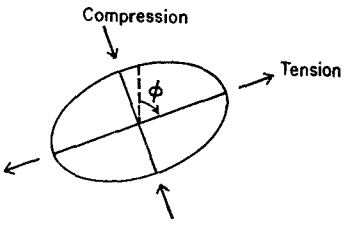


(b) (c)

FIG. 11. Deformed fluid drop in a suspension undergoing Poiseuille flow. (*a*) Coordinates. (*b*) Coordinates for Couette flow: $(X', Y')$ and $(X, Y)$ are the respective axes before and after rotation of the field through an angle $-\delta$. (*c*) Forces acting on drop.

Let $P_{x'}(\phi)\, d\phi$ and $P_{y'}(\phi)\, d\phi$ be the elements of force in the interval $d\phi$ at $\phi$. We then have

$$P_{x'}(\phi)d\phi = 2d\phi \int_0^{\pi/2} b^2 p_{rx'} \sin\theta \, d\theta.$$

Hence

$$P_{x'}(\phi) = 2b^2 \int_0^{\pi/2} p_{rx'} \sin\theta \, d\theta; \qquad [26a]$$

and similarly

$$P_{y'}(\phi) = 2b^2 \int_0^{\pi/2} p_{ry'} \sin\theta \, d\theta. \qquad [26b]$$

Substituting from [25] and integrating we obtain

$$P_{x'}(\phi) = \epsilon G[1 + \beta \sin^2 \phi] \cos \phi \qquad [27a]$$

$$P_{y'}(\phi) = \epsilon G[1 + \beta \cos^2 \phi] \sin \phi, \qquad [27b]$$

where

$$\epsilon = \frac{5\pi p \eta_2 b^2}{4(p + 1)} \quad \text{and} \quad \beta = \frac{12}{5p}.$$

The theory of Cerf (24) shows that owing to rotation in Couette flow the principal axes of deformation are rotated beyond $\phi = \pm\pi/4$ through an angle $\delta$ given by the last term of [23]. We may consider this to occur by rotating the Couette field through the angle $-\delta$, thus leaving the particle fixed in space (Fig. 11*b*). We now wish to calculate the net force acting along the axis $YY$. The component of force acting along the $YY$ axis at $\phi$ is then given by

$$P_y(\phi) = P_{y'}(\phi) \cos \delta + P_{x'}(\phi) \sin \delta. \qquad [28]$$

For small deformation where $\delta$ is small this may be written as

$$P_y(\phi) = P_{y'}(\phi) - \delta P_{x'}(\phi). \qquad [29$$

The velocity gradient around the particle is now given by

$$\begin{aligned} G &= G_0 + ky \\ &= G_0 + kb \cos (\phi + \delta). \end{aligned} \qquad [30]$$

The deformation may be described by the polar equation (9).

$$r(\phi) = b(1 + D \sin 2\phi). \qquad [31]$$

Rewriting [30] in polar form we obtain

$$\begin{aligned} G &= G_0 + kr(\phi) \cos (\phi + \delta) \\ &= G_0 + kb(1 + D \sin 2\phi) \cos \phi - \delta kb(1 + D \sin 2\phi) \sin \phi. \end{aligned} \qquad [32]$$

The net force is therefore

$$F_{rr} = \int_0^{2\pi} [P_y(\phi) - \delta P_x(\phi)]\, d\phi. \qquad [33]$$

Substituting for $P_y(\phi)$ and $P_x(\phi)$ from [27] yields

$$\begin{aligned} F_{rr} = \epsilon \int_0^{2\pi} &[\sin \phi + \beta \cos^2 \phi \sin \phi] \\ &\cdot [G_0 + kb(1 + D \sin 2\phi) \cos \phi - kb\delta(1 + D \sin 2\phi) \sin \phi]\, d\phi \\ &- \epsilon\delta \int_0^{2\pi} [\cos \phi + \beta \sin^2 \phi \cos \phi] \\ &\cdot [G_0 + kb(1 + D \sin 2\phi) \cos \phi - kb\delta(1 + D \sin 2\phi) \sin \phi]\, d\phi. \end{aligned}$$

Upon integration and reduction this finally yields

$$F_{rr} = -\frac{5\pi^2 k b^3 \eta_2 D}{2(p+1)}\left[\left(1+\frac{2p}{5}\right)\left(p+\frac{3}{5}\right) - \tfrac{1}{4}\left(p+\frac{6}{5}\right)\right]. \qquad [34]$$

Thus there is a net force acting to push the drop to a lower gradient. When $D = 0$, as in the case of a rigid sphere, $F_{rr} = 0$, thus accounting for the observed difference in behavior between rigid and deformable particles. Likewise $F_{rr} = 0$ when $k = 0$, as in Couette flow, and hence there is no tendency to migrate across the planes of shear. It should be mentioned that recent experiments conducted in this laboratory have revealed the presence of drop migration in Couette flow. This occurred when the deformed drop, suspended in a liquid contained in the annulus between two counter-rotating cylinders (5), was situated close to either wall of the apparatus, migration taking place towards the center of the annulus. This result may be attributed to interaction between the drop and the wall leading to a gradient in $G$ and a nonvanishing value of $k$. As might be expected from the results obtained in Poiseuille flow, migration of rigid spheres was not observed. Further experiments are in progress and these will be reported in a subsequent paper.

Assuming the drop is propelled radially with Stokes velocity (corrected for internal circulation) we have

$$F_{rr} = 6\pi\eta_2 b f_2(p)\left(\frac{dr}{dt}\right), \qquad [35]$$

where $(dr/dt)$ is the migration velocity and $f_2(p)$ is the Hadamard correction factor (25) given by

$$f_2(p) = \frac{(p+\tfrac{2}{3})}{(p+1)}. \qquad [36]$$

Equating [34] and [35] and substituting for $D$ from [20] finally yields

$$\frac{dr}{dt} = -\frac{\pi\eta_2}{48\gamma} f_3(p) k^2 b^3 r, \qquad [37]$$

which upon integration gives

$$\log_e \frac{r}{r_0} = -\frac{\pi\eta_2}{48\gamma} f_3(p) k^2 b^3 t, \qquad [38]$$

where $f_3(p)$ is given by

$$f_3(p) = \frac{3(19p+16)\left(8p^2+\frac{99p}{5}+6\right)}{(16p+16)(3p+2)}, \qquad [39]$$

$r_0$ being the radial distance of the particle center at $t = 0$. Eq. [39] is a better approximation than that given in a preliminary communication (27).

Values of the initial $(dr/dt)$ calculated from Eq. [37] are compared with those measured in System 6, Table VIII. Figure 12 is a summary plot of the data according to [38] showing that the experimental points obtained at different $b$ and $Q$ lie on a single curve, initially linear but eventually deviating from the line. Similar results were obtained in Systems 7 and 8. The values of the *measured/calculated* initial slope are shown in Table IX.

The results show that while in a given system the radial velocity varies

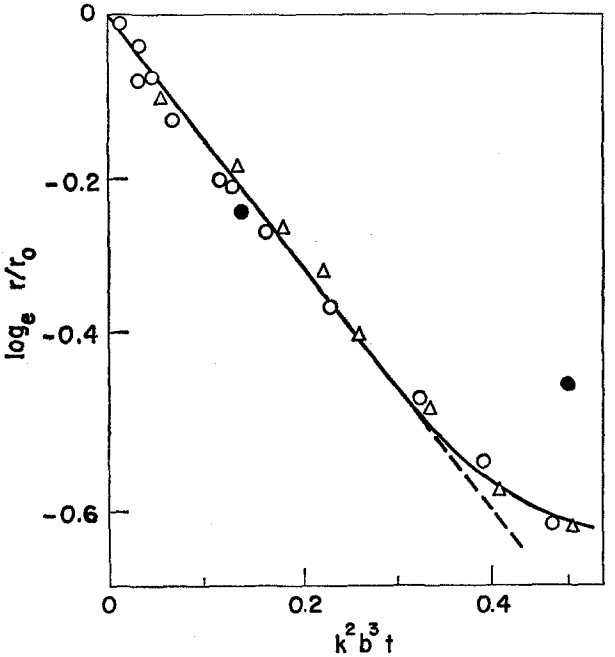


FIG. 12. Axial migration of fluid drops in System 6, $R = 0.400$ cm. Plot of $\log_e r/r_0$ against $k^2b^3t$ according to [38] for the data previously shown in Fig. 10. Open circles: $Q = 0.0356$ cm.$^3$ sec.$^{-1}$. Triangles: $Q = 0.0712$ cm.$^3$ sec.$^{-1}$. Closed circles: $Q = 0.142$ cm.$^3$ sec.$^{-1}$.

TABLE IX

*Measured and Calculated Migration of Deformable Drops*

| System | $\log_e \frac{r}{r_0} \Big/ k^2b^3t$ | | Ratio $\frac{\text{meas.}}{\text{calc.}}$ Slope[b] |
|---|---|---|---|
| | Meas. | Calc.[a] | |
| 6 | −1.6 | − 1.0 | 1.60 |
| 7 | −2.6 | − 4·0 | 0.65 |
| 8 | −1.6 | −17·6 | 0.09 |

[a] Equation [38] using $\gamma$ calculated from deformation [20].

[b] $\frac{\pi\eta_2 f_3(p)}{48\gamma}$ from [38]

as $(k^2b^3r)$, the exact value of $f_3(p)$ differs somewhat from [39]. It has been found that considerable variation in $f_3(p)$ results from varying the boundary conditions assumed in deriving [34], although in all cases considered the dimensionless group $(kb^3\eta_2 D)$ appears. The conclusion is drawn that the general principles of the theory are correct although its details are not.

In System 10 the slope of the plot of [38] decreased with increasing deformation. This can be explained by the negative deviation from [20] which occurs at low deformation (Fig. 8).

The theory given above for the migration of single particles cannot be expected to hold in suspensions of appreciable concentration where the presence of other particles may be expected to give rise to the following effects:

*a*). *Collisions.* It has been shown (26) in Couette flow that in a collision between two deformed drops the angle of separation of the line of particle centers ($\phi'$) is less than the angle of contact ($-\phi$), thus resulting in a displacement along the $Y$-axis of one of the drops. Since collisions in Poiseuille flow must occur on the axial side of the drop having the lower velocity, the drop moving with the greater velocity will be displaced towards the tube axis. This provides an additional possible mechanism for axial migration.

*b*). *Plug flow.* Axial migration is probably impeded by the presence of other particles until a state of equilibrium is reached with the drops confined to the core of the tube surrounded by a layer of suspending liquid; this may lead to plug flow in the central core. Owing to the compression of the plug the drops would be deformed, the deformation increasing with increasing flow rate as the plug is further compressed. Such behavior was observed in the flow of aqueous pulp fiber suspensions (15) where the elastic network of fibers constituting the plug was demonstrated to be under radial compression since, when flow ceased, it sprang back against the wall of the tube. As the flow rate was further increased, turbulent flow developed first in the water layer and finally in the plug as well. Similar behavior has been deduced from indirect measurements in blood flow (28).

Finally, the theory given above shows that the forces acting on rigid rotating rods would be expected to produce migration towards the tube axis in the quadrant $\phi = 0°$ to $90°$ and an equal migration towards the wall in the quadrant $\phi = -90°$ to $0°$ (and vice versa for discs), as a result of which the center of rotation would describe a sinusoidal path. The fact that such behavior was not observed experimentally would indicate that the amplitude of the radial displacements is very small. This, however, remains to be studied further.

## Summary

The motions of single rigid spheres, rods, and discs, and of fluid drops suspended in liquids undergoing Poiseuille flow have been studied.

With the exception of effects due to interaction with the wall and neglect of particle size, the angular rotation of the spheres, rods, and discs was in good agreement with the theory of Jeffery, provided that the equivalent axis ratio $r_e$ was used instead of the particle axis ratio $r_p$.

The periods of rotation of the particles near the wall of the tube were greater than those calculated from the theory. In the case of spheres quantitative agreement with the theory of Vand for rotation in proximity to a wall was obtained.

The deformation and burst of liquid drops were in quantitative agreement with the theories of Taylor and Cerf for small deformation.

The existence of axial migration in the case of fluid drops and its absence with rigid particles was demonstrated. The measured rate of migration of drops agreed with an approximate theory based on the radial variation of the velocity gradient.

## References


1. Trevelyan, B. J., and Mason, S. G., *J. Colloid Sci.* **6,** 354 (1951).
2. Mason, S. G., and Manley, R. St. J., *Proc. Roy. Soc. (London)* **A238,** 117 (1956).
3. Bartok, W., and Mason, S. G., *J. Colloid Sci.* **12,** 243 (1957).
4. Forgacs, O. L., and Mason, S. G., *J. Colloid Sci.* **14,** 457 (1959).
5. Rumscheidt, F. D., and Mason, S. G., *J. Colloid Sci.* **16,** 238 (1961).
6. Goldsmith, H. L., and Mason, S. G., *J. Fluid Mech.* (1961).
7. Jeffery, G. B., *Proc. Roy. Soc. (London)* **A102,** 161 (1922).
8. Taylor, G. I., *Proc. Roy. Soc. (London)* **A138,** 41 (1932).
9. Taylor, G. I., *Proc. Roy. Soc. (London)* **A146,** 501 (1934).
10. Bayliss, L. E., *in* Frey Wyssling: "Deformation and Flow in Biological Systems." Chapter VI. "Rheology of blood and lymph." Interscience Publishers, New York, 1952.
11. Starkey, T. V., *Brit. J. Appl. Phys.* **7,** 52 (1956).
12. Segre, G., and Silberberg, A., *Nature* **189,** 209 (1961).
13. Fahraeus, R., *Physiol. Revs.* **9,** 241 (1929).
14. Vejlens, G., *Acta Pathol. Microbiol. Scand. Suppl.* **No. 33** (1938).
15. Forgacs, O. L., Robertson, A. A., and Mason, S. G., *Pulp & Paper Mag. Can.* **59,** 5, 117 (1958).
16. Starkey, T. V., *Brit. J. Appl. Phys.* **7,** 448 (1956).
17. Whitmore, R. L., "Rheology of Disperse Systems," p. 49. Pergamon Press, (London), 1959.
18. Brenner, H., and Happel, J., *J. Fluid Mech.* **4,** 195 (1958).
19. Happel, J., and Byrne, B. J., *Ind. Eng. Chem.* **46,** 1181 (1954).
20. Bartok, W., Ph.D. Thesis, McGill University, Montreal, 1957.
21. Vand, V., *J. Phys. & Colloid Chem.* **52,** 300 (1948).
22. Vand, V., *J. Phys. & Colloid Chem.* **52,** 277 (1948).
23. Oseen, C. W., "Hydrodynamik." Leipzig, 1927.
24. Cerf, R., *J. chim. phys.* **48,** 59 (1951).
25. Hadamard, M. J., *Compt. rend.* **152,** 1735 (1911).
26. Allan, R. S., and Mason, S. G., *J. Colloid Sci.* **17,** 383 (1962).
27. Goldsmith, H. L., and Mason, S. G., *Nature* **190,** 1095 (1961).
28. Coulter, N. A., and Pappenheimer J. R., *Am. J. Physiol.* **159,** 401 (1949).